nature materials

ARTICLES

https://doi.org/10.1038/s41563-020-0631-x

Check for updates

Atomically thin half-van der Waals metals enabled by confinement heteroepitaxy

Natalie Briggs[1,2,3,14], Brian Bersch[1,2,14], Yuanxi Wang[2,3,14], Jue Jiang[4], Roland J. Koch[5,6], Nadire Nayir[3,7], Ke Wang[8], Marek Kolmer[9], Wonhee Ko[9], Ana De La Fuente Duran[1], Shruti Subramanian[1,2], Chengye Dong[1,2], Jeffrey Shallenberger[8], Mingming Fu[9], Qiang Zou[9], Ya-Wen Chuang[4], Zheng Gai[9], An-Ping Li[9], Aaron Bostwick[5], Chris Jozwiak[5], Cui-Zu Chang[4], Eli Rotenberg[5], Jun Zhu[2,4], Adri C. T. van Duin[1,3,7,8,10,11,12], Vincent Crespi[2,3,4,8] and Joshua A. Robinson[1,2,3,8,13] ✉

Atomically thin two-dimensional (2D) metals may be key ingredients in next-generation quantum and optoelectronic devices. However, 2D metals must be stabilized against environmental degradation and integrated into heterostructure devices at the wafer scale. The high-energy interface between silicon carbide and epitaxial graphene provides an intriguing framework for stabilizing a diverse range of 2D metals. Here we demonstrate large-area, environmentally stable, single-crystal 2D gallium, indium and tin that are stabilized at the interface of epitaxial graphene and silicon carbide. The 2D metals are covalently bonded to SiC below but present a non-bonded interface to the graphene overlayer; that is, they are 'half van der Waals' metals with strong internal gradients in bonding character. These non-centrosymmetric 2D metals offer compelling opportunities for superconducting devices, topological phenomena and advanced optoelectronic properties. For example, the reported 2D Ga is a superconductor that combines six strongly coupled Ga-derived electron pockets with a large nearly free-electron Fermi surface that closely approaches the Dirac points of the graphene overlayer.

Major advances in fundamental science have resulted from the exfoliation, stacking and encapsulation of atomically thin 2D layers[1]. The next step towards a technological impact of 2D layers and heterostructures is to transition sophisticated 'pick and place' devices to a wafer-scale platform. However, the sensitivity of 2D systems to interfacial reactions and environmental influences—especially for 2D metals or small-gap semiconductors—poses challenges for large-scale integration. Very few metals resist degradation of their top few atomic layers upon environmental exposure, and for a 2D metal, these layers constitute the entire system. A general platform for producing environmentally stable and wafer-scale 2D metals that are not prone to interfacial interactions would represent a significant advance. Inspired by the success of wide-bandgap 2D gallium nitride[2], we focus on the metal alone and demonstrate a platform dubbed confinement heteroepitaxy (CHet), where the interface between epitaxial graphene (EG) and silicon carbide (SiC) stabilizes crystalline 2D forms of group III (Ga, In) and group IV (Sn) elements. Defect engineering of the graphene overlayer enables uniform, large-area intercalation at the high-energy SiC/EG interface; this interface then templates intercalant crystallization at a thermodynamically defined number of atomic layers. The unreactive nature of as-grown EG on SiC (graphene plus buffer layer) results in the EG performing multiple services: it only partially passivates the SiC surface underneath, thereby sustaining the high-energy interface that drives intercalation; it lowers the energy of the (otherwise exposed) upper surface of the metal, thus facilitating 2D morphologies; and it protects the newly formed 2D metal from environmental degradation after intercalation through in situ healing of the graphene defects. The stability of these 2D metals in air over a period of months greatly facilitates ex situ characterization and enables facile processing and device fabrication. Competing methods to obtain thin, single-crystal metal films are specific to certain metallic species (for example Au (ref. [3]) or TiN (ref. [4])) and generally produce thicker layers of a few nanometres without in situ encapsulation, whereas CHet produces stable, atomically thin crystalline 2D forms of diverse metals that do not otherwise exist in nature.

Unlike traditional EG intercalation methods[5–8], CHet (Fig. 1a) uses plasma-treated EG and high-pressure (300 Torr) thermal evaporation to create continuous films of crystalline 2D metals. Nominally monolayer EG is grown by silicon sublimation from 6H-SiC (0001) (ref. [9]), after which exposure to an oxygen plasma generates defects in the EG layers. Metallic precursors such as Ga, Sn and In situated in a crucible directly beneath the EG are then heated with the EG/SiC to 700–800 °C. The vaporized metal diffuses through EG defects to reach the EG/SiC interface. X-ray photoelectron spectroscopy

[1]Department of Materials Science and Engineering, The Pennsylvania State University, University Park, PA, USA. [2]Center for 2-Dimensional and Layered Materials, The Pennsylvania State University, University Park, PA, USA. [3]2-Dimensional Crystal Consortium, The Pennsylvania State University, University Park, PA, USA. [4]Department of Physics, The Pennsylvania State University, University Park, PA, USA. [5]Advanced Light Source, Lawrence Berkeley National Laboratory, Berkeley, California, USA. [6]The Molecular Foundry, Lawrence Berkeley National Laboratory, Berkeley, California, USA. [7]Department of Mechanical Engineering, The Pennsylvania State University, University Park, PA, USA. [8]Materials Research Institute, The Pennsylvania State University, University Park, PA, USA. [9]Center for Nanophase Materials Sciences, Oak Ridge National Laboratory, Oak Ridge, TN, USA. [10]Department of Chemistry, The Pennsylvania State University, University Park, PA, USA. [11]Department of Engineering Science and Mechanics, The Pennsylvania State University, University Park, PA, USA. [12]Department of Chemical Engineering, The Pennsylvania State University, University Park, PA, USA. [13]Center for Atomically Thin Multifunctional Coatings, The Pennsylvania State University, University Park, PA, USA. [14]These authors contributed equally: Natalie Briggs, Brian Bersch, Yuanxi Wang. ✉e-mail: jrobinson@psu.edu

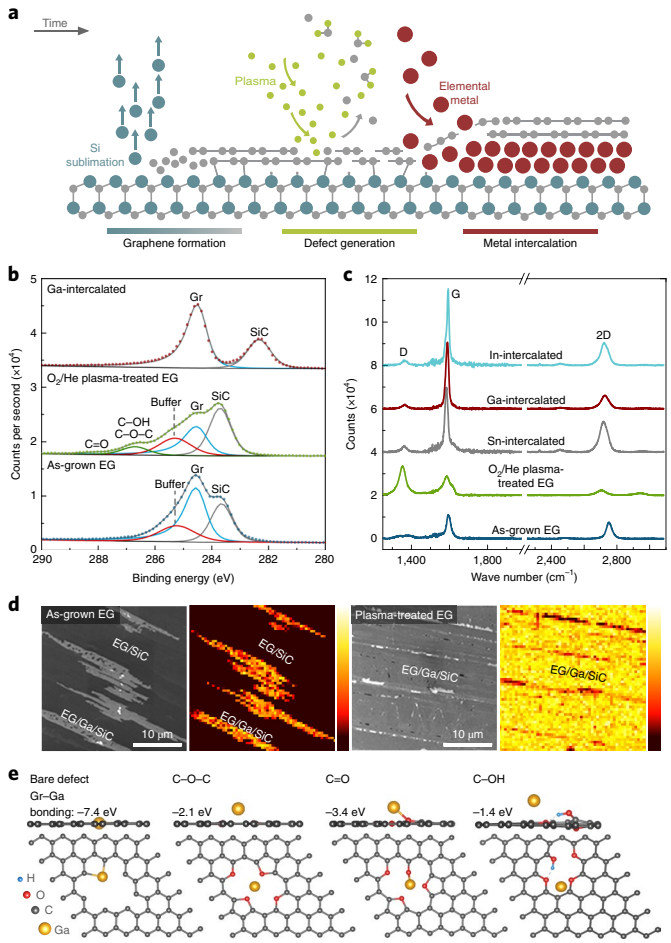

Fig. 1 | CHet with defect-engineered epitaxial graphene. a, Schematic of CHet showing EG growth, O_2/He plasma treatment and intercalation steps. **b**,**c**, XPS showing C 1*s* for as-grown EG (bottom), O_2/He plasma-treated EG (middle), and Ga-intercalated, O_2/He plasma-treated EG (top) demonstrating the creation and annihilation of C–O bonds during CHet; this is confirmed by **c**, Raman spectroscopy of as-grown EG, O_2/He plasma-treated EG and metal-intercalated, O_2/He plasma-treated EG, where the defect peak (D peak) intensity is dramatically reduced as a result of the intercalation process. SiC Raman spectra are subtracted from the Raman data shown in **c**. The Gr label in **b** corresponds to the blue fitted peak, which denotes graphene layers in the C 1*s* spectra. **d**, SEM and accompanying Ga AES maps of Ga-intercalated, as-grown EG and Ga-intercalated, O_2/He plasma-treated EG. Defects formed due to plasma treatments lead to significantly improved intercalation uniformity. The AES colour scales show low (dark) to high (light) Ga signal across the mapped regions. **e**, DFT modelling of Ga atoms on graphene sheets containing unpassivated and passivated defects. DFT models of Ga on graphene sheets containing defects passivated with C–O–C, C=O, and C–OH suggest that oxygen termination provides favourable energies for metal attraction and intercalation through the graphene sheet. The Ga binding energy to each defect is shown in each model.

(XPS; Fig. 1b) and Raman spectroscopy (Fig. 1c) reveal how the EG defects evolve during CHet. O_2/He plasma treatments create defects in the EG that contain C=O and C–OH or C–O–C bonds visible in the C 1*s* spectra (Fig. 1b)[10,11]; these defects correlate with a ×15 increase in the Raman D/G intensity ratio (I_D/I_G; Fig. 1c)[12]. Upon metal intercalation, signatures of carbon–oxygen bonding and the EG buffer layer peak disappear from the C 1*s* region (Fig. 1b), and a metallic Ga 3*d* peak appears (Supplementary Fig. 1). Ultimately, metal intercalation (Ga, In or Sn) releases the buffer layer[5–7] and removes carbon–oxygen bonding. XPS signatures remain stable even after more than eight months in air (Supplementary Fig. 2). Intercalation also yields a pronounced (~×5) decrease in I_D relative to plasma-treated EG, and a ×3–4 and ×1–2 increase in I_G and I_{2D}, respectively, relative to as-grown EG (Fig. 1c). The decreased I_D, lack of D′ and D+G modes, loss of carbon–oxygen bonding and air stability of the resulting 2D metals all suggest that the EG heals during intercalation at elevated temperatures[13–15] and subsequently acts as a barrier to oxidation post-synthesis. The strengthening of I_G and I_{2D} after intercalation may be attributed to metal/EG charge transfer and/or plasmon resonance[16–18]. A comparison of Auger electron spectroscopy (AES; Fig. 1d and Supplementary Fig. 3) and Raman mapping (Supplementary Fig. 4) of EG/Ga samples prepared using pristine versus plasma-treated EG reveals that plasma treatments greatly increase the lateral coverage of intercalated Ga. Beyond a simple increase in intercalation sites, first-principles calculations indicate that Ga/EG bonding is strengthened with increasing vacancy size, where large, unpassivated defects bond covalently with Ga (Fig. 1e and Supplementary Fig. 5). First-principles calculations suggest that the termination of multivacancy graphene defects with oxygen moieties facilitates metal adhesion and transport to the underlying EG/SiC interface through intermediate metal binding energies that are weaker than those of unpassivated vacancies but stronger than those for hydroxyl terminations or the basal plane (Fig. 1e and Supplementary Fig. 5).

Two-dimensional Ga, In and Sn are one to three atomic layers thick and registered to the SiC substrate (Fig. 2a,c,e). The dominant thickness observed can be explained by first-principles equilibrium-phase stability calculations (Fig. 2b,d,f and Supplementary Fig. 6) that predict the layer number as a function of the metal chemical potential. Based on first-principles calculations, the strong metal–SiC bonding stabilizes a 2D metal compared to the bulk 3D form, but this advantage is diluted by successive thickening of the intercalant so that the bulk phase is preferred beyond a certain thickness. These calculations predict a stability range of one to three layers for Ga, one to two layers for In and one layer for Sn, all in encouragingly close agreement with scanning transmission electron microscopy (STEM) images (Fig. 2a,c,e), which display three layers of Ga, two of In and one to two layers of Sn (in the case of Sn, the blurring of the second Sn layer indicates a lower structural stability for this layer). This close correspondence suggests near-equilibrium growth conditions during CHet, that is, a relatively high metal atom mobility, which is supported by the uniform metal coverage achieved. The high energy of the initial EG/SiC interface, which follows from the ineffectiveness of EG in terminating SiC dangling bonds, provides a strong thermodynamic driving force for 2D metal formation, suggesting a broader applicability of CHet to support additional species as 2D metals. The metal thicknesses shown in Fig. 2a,c,e are uniform across the terraces of SiC, although some SiC terraces show uniform two-layer Ga.

An epitaxial relationship of the 2D metals to the SiC substrate is further supported by the observation in low-energy electron diffraction (LEED) of EG and SiC patterns, without distinct spots corresponding to a structurally unique intercalant layer (Fig. 2g and Supplementary Fig. 8). The SiC diffraction pattern is shared by the metal. The 2.72 Å lateral Ga spacing observed via STEM also closely matches that of SiC (Fig. 2a and Supplementary Fig. 9). First-principles structural optimization provides further insights into the epitaxial relationship of Ga to SiC (0001). Structural relaxations were performed for one to three layers of Ga initialized at sites projecting onto the silicon, carbon and/or hollow sites of SiC (Fig. 2h, Supplementary Figs. 10,11 and Supplementary Table 1). Adding a top bilayer graphene affects only the band fillings without changing the relative stability of the Ga structures (Supplementary Table 1), therefore bilayer graphene is not considered in these

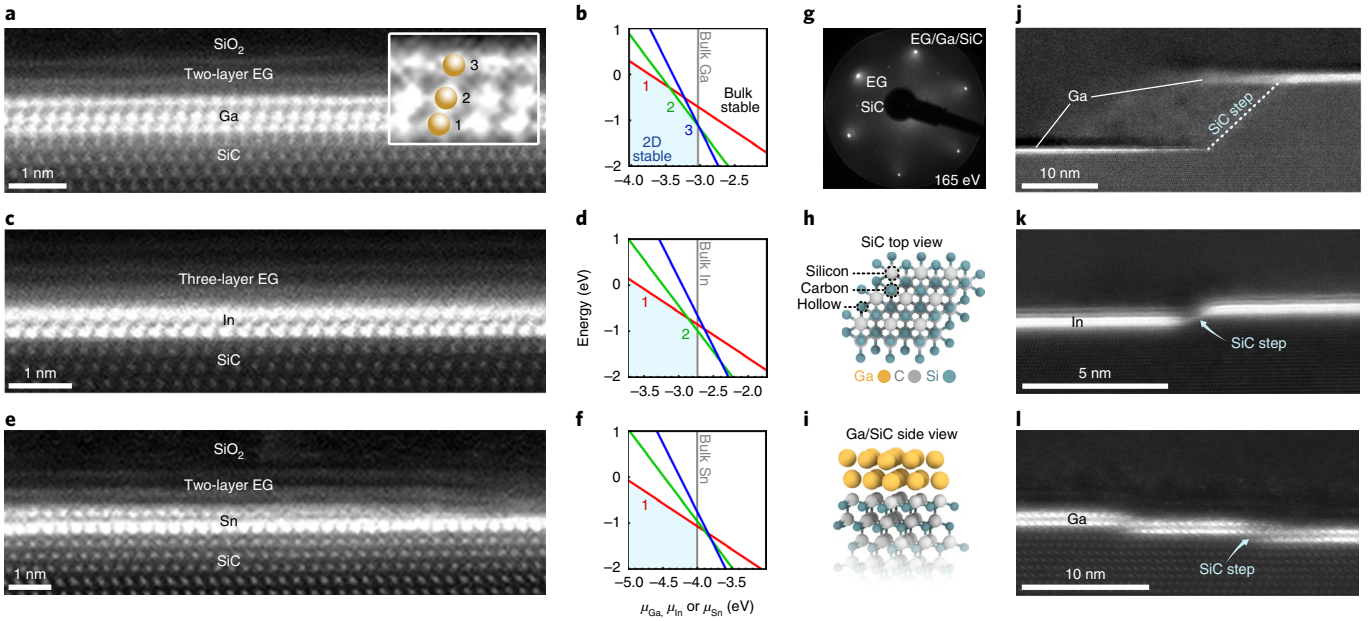

Fig. 2 | Atomic structure of CHet-grown 2D metals. a, Cross-sectional STEM showing three layers of Ga between EG and SiC. The inset shows the different interlayer spacings of the Ga layers. **b**, Corresponding energy minimization calculations showing preferred Ga layer numbers. **c**–**f**, Cross-sectional STEM and layer-number calculations for In and Sn. EDS (Supplementary Fig. 7) confirms that intercalant layers match the respective precursor elements and are not oxidized. The grey, vertical lines in **b**, **d** and **f** indicate the metal chemical potential of the bulk metal, and the red, green and blue lines indicate the energy as a function of chemical potential for one, two and three layers, respectively. The lowest line at a given potential indicates the layer number of the ground state. **g**, Acquired LEED pattern for EG/Ga/SiC indicating the presence of EG and SiC with no additional spots for a unique Ga structure (or In or Sn structure; see Supplementary Fig. 8), indicating the Ga is lattice matched to EG or SiC. **h**,**i**, Top-down schematic (**h**) of hexagonal SiC with silicon, carbon and hollow sites labelled; intercalated Ga layers exhibit an ABC stacking over the SiC substrate (**i**). **j**–**l**, Step bunching in the SiC surface can lead to discontinuities in the 2D metals, necessitating that SiC steps be only a few atoms in height to maintain the structural and electrical continuity of the 2D metal films.

structural stability calculations. The ground-state locations for the first, second and third layers of Ga are above the silicon (Ga_{Si}), carbon (Ga_C) and hollow (Ga_{hollow}) sites, respectively (Fig. 2i). This ABC stacking resembles a face-centred cubic (fcc) lattice cleaved along the (111) plane, matching the hexagonal arrangement of SiC (0001), and is possibly related to the metastable distorted fcc phase of Ga(III) (ref. [19]). The Ga registry weakens for increased metal thickness: the Ga_{Si} stacking site for single-layer Ga is 0.14 eV per unit cell (that is, per 8.30 Å^2), more stable than that of Ga_C or Ga_{hollow}, but the ground states of Ga multilayers are preferred by only 0.05 eV against competing phases. Cross-sectional STEM (Fig. 2a, inset) supports the calculated evolution with increasing thickness, where the interlayer spacing between the first and second Ga layers (2.19 Å) is significantly smaller than that between the second and third (2.36 Å). Density functional theory (DFT) results show a pronounced shift from largely covalent bonding in the bottom Ga layer (templated against SiC) to comparably strong but more metallic bonding between the upper Ga layers and much weaker interaction between the upper Ga layer and the graphene overlayer (Supplementary Table 1). Experimentally, epitaxy and metal continuity are interrupted by large steps in the SiC surface (Fig. 2j), while smaller steps (Fig. 2k) are less disruptive and single-atom steps (Fig. 2l) are metal-continuous and appear to maintain epitaxy across the step.

The structural quality of 2D Ga is reflected in the excellent agreement of angle-resolved photoemission spectroscopy (ARPES) measurements with calculations of the structurally optimized epitaxial system (Fig. 3a, also Supplementary Fig. 12 for 2D In). The high valence electron count of *p*-block metals and the small lateral unit cell of epitaxial 2D Ga yield an exceptionally large *s*-band Fermi velocity of 2×10^6 m s^{-1}, comparable to that of bulk Al and Ga (assuming a free-electron model)[20] or In on Si(111) (ref. [21]) and substantially larger than the band velocity of graphitic π states[22,23]. The calculated band structure (Fig. 3b) shows colour-coded projections of the total wavefunction onto the plane-wave components of the graphene (black) and Ga/SiC (blue) primitive cell, where bands are unfolded from the supercell Brillouin zone[24]. The most prominent features are three avoided crossings between *s* and *p* Ga bands, one along Γ-M_{Ga} and two along Γ-K_{Ga} (comparing with a freestanding frozen bilayer of Ga (Supplementary Fig. 13), the Ga *s*-band starts ~9 eV below the Fermi level). A large Ga-derived near-free-electron-like Fermi surface (Fig. 3c,d) closely approaches the graphene Dirac points at K_{gr} and K'_{gr} with further electron pockets around the corners of the Ga Brillouin zone. The position of the graphene Dirac point 0.2–0.3 eV below the Fermi level (Supplementary Fig. 14) indicates that Ga (or In, Supplementary Fig. 12) electron-dopes graphene by $8–10\times10^{12}$ cm^{-2}. This is supported by the Fermi surface of bilayer Ga/SiC calculated without graphene (Fig. 3e) where the Fermi level is upshifted by 0.4 eV to be consistent with the measured ARPES band alignment (see Supplementary Fig. 11); this artificial upshift is not needed when using hybrid functionals, which generally yield more accurate band alignments (see Supplementary Information for details on the supercell strain imposed in the calculations). Finally, the measured Fermi surface clearly shows that the graphene Brillouin zone is rotated 30° from the underlying Ga/SiC zone, providing direct evidence of the orientational epitaxy between Ga and SiC.

The air stability of 2D metals formed by CHet enables ex situ transport measurements without complex capping methodologies. A co-linear four-point-probe configuration with In dot contacts reveals a largely metallic behaviour for 2D Ga on small-step SiC from room temperature down to 4 K, below which a sharp,

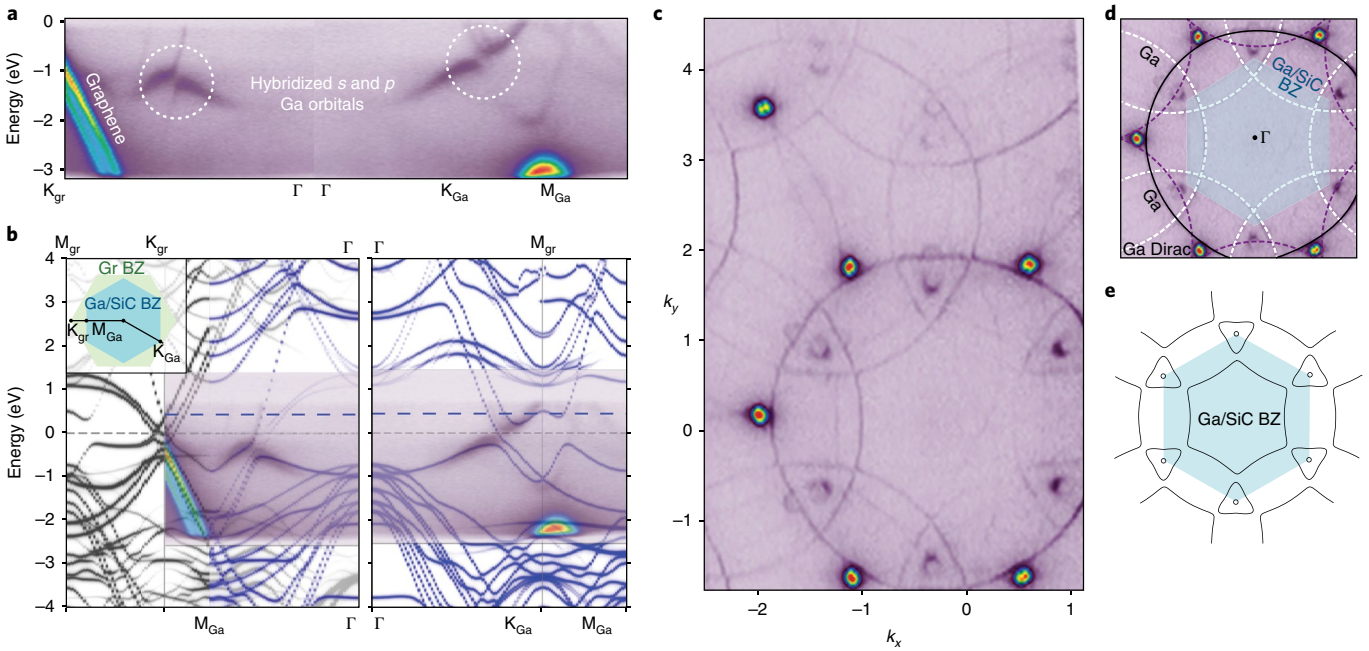

Fig. 3 | Electronic structure of CHet-grown 2D Ga. a,**b**, Measured ARPES spectra for EG/Ga/SiC showing EG and Ga bands near M_{Ga} and K_{Ga} (**a**) and calculated band structure in black and blue overlaid with measured ARPES (purple) (**b**). The effective unfolded band structures of 2×2 graphene + $\sqrt{3}\times\sqrt{3}$ R30º bilayer Ga/SiC along the Γ-M_{Ga} (Γ-K_{gr}) and the Γ-K_{Ga} (Γ-M_{gr}) directions are projected onto graphene (black) and Ga/SiC (blue), as indicated by the Brillouin zone (BZ) paths in the inset (M_{gr} in the left panel and M_{Ga} on the right are from repeated zones). ARPES measurements along the same paths are superimposed. **c**,**d**, ARPES-measured Fermi surface showing nearly free-electron-like circular contours, where k_x and k_y are the electron crystal momenta in the in-plane directions. Superimposed black, white and purple circles in **d** correspond to nearly free-electron-like circular contours from Ga and are drawn to aid in the comparison of the experimental data with calculated data. **e**, DFT-calculated Fermi surface of bilayer Ga/SiC with the Fermi level shifted (to the blue dashed line in panel **b**) to match the measured band filling.

four-order-of-magnitude drop in resistance occurs (Fig. 4a). As defined in the Methods section, $T_c^{onset} = 3.95$ K and $T_c^{zero} = 3.2$ K, values that are higher than those in bulk orthorhombic α-Ga (1.08 K)[25], similar to those of metastable monoclinic β-Ga (5.9–6.5 K) and below those of metastable amorphous Ga (8.4 K)[26–28]. As expected, the transition drops and broadens with increasing perpendicular magnetic field $B_\perp$ (Fig. 4b). Resistance (R) versus $B_\perp$ indicates $B_c = 130$ mT at 2 K with a corresponding coherence length ξ_0 ~50 nm (Fig. 4c and Methods). A linear extrapolation of $B_c(T)$ from $R(B)$ suggests a zero-Kelvin critical field $B_{c0} \approx 260$ mT and ξ_0 ~36 nm, higher than that of α-Ga ($B_{c0} \approx 6$ mT)[25] and β-Ga ($B_{c0} \approx 54$ mT (ref. [28]); Supplementary Fig. 15a). Considering the very high Fermi velocity and moderate T_c, the system is likely not in the clean limit. Scanning tunnelling microscopy/spectroscopy show quite uniform differential tunnelling conductance (dI/dV) spectra at multiple locations on the sample (Fig. 4d,f and Supplementary Fig. 15). A superconducting gap with well-defined coherence peaks at ±0.6 meV is seen at 2.2 K (Fig. 4h) and disappears at ~3 K, below the transport T_c (Fig. 4g), perhaps due to a moderately reduced proximity-induced superconducting order parameter in the two- to three-layer EG overlayer[29]. The observation of a significant superconducting order parameter at the upper EG surface bodes well for the formation of superconducting heterostructures via the proximity effect.

When crystallographic steps on SiC (0001) are less than 1 nm tall (Fig. 2k,l), transport measurements that orient the current parallel or perpendicular to the steps have similar T_c^{onset} (~4 K) and T_c^{zero} (~3.2 K) values (Fig. 4i). Although steps more than 5 m tall (Figs. 2j,4j) yield a similar T_c^{onset} of ~3.8 K for both directions, only parallel transport displays a fully developed superconducting transition with a T_c^{zero} of ~2.5 K, suggesting that transport perpendicular to large steps encounters a finite series resistance at the steps. Small-step 2D Ga exhibits a Berezinskii–Kosterlitz–Thouless (BKT) transition temperature[30] of $T_{BKT} = 3.1$ K (2.9 K) for transport parallel (perpendicular) to the SiC steps (Supplementary Fig. 17), indicating a largely isotropic 2D superconducting transition in these samples. Note that I–V measurements up to the critical current (I_c) are limited by the experimental setup, and T_{BKT} is likely closer to 3.88 K (Supplementary Fig. 17) if extracted from curves closer to I_c. Full $R(T)$ and $R(B)$ curves for 'large-step' 2D Ga are provided in Supplementary Fig. 18. Epitaxial graphene synthesis must limit step bunching to ensure uniform superconducting films with isotropic transport. SiC step height and bunching can be mitigated by reducing the temperature of the pre-EG-growth H_2 etch step[31], or through the delivery of carbon to the SiC surface during EG growth to promote buffer layer nucleation and suppress mass transport across SiC that leads to step formation[32,33].

When considering the electronic origin of the superconductivity in 2D Ga/SiC, each of the constituent materials appear to be poor superconductors: SiC is semiconducting, EG is not as heavily doped (Supplementary Fig. 14) as in graphite intercalation compound superconductors, and 2D Ga exhibits nearly free-electron characteristics that would not lead to a substantial T_c, since electron–lattice interactions are weak in nearly free-electron metals. We show, using first-principles calculations, that another Fermi surface manifold—small electron pockets around K—supports superconductivity. Using DFT, we calculate the electronic densities of states (DOSs) near the Fermi level for α-Ga, β-Ga and one- to three-layer 2D Ga (Fig. 5a,b) and also the Eliashberg spectral function $\alpha^2F(\omega)$ for three-layer $Ga_{Si}Ga_CGa_C$ epitaxial to SiC without the graphene cap (Methods and Supplementary Fig. 19). α-Ga contains Ga dimers whose incipient covalency suppresses the DOS near the Fermi level, while β-Ga recovers a more nearly free-electron-like behaviour (Fig. 5a). Two-layer and three-layer Ga/SiC (Fig. 5b) exhibit a DOS at E_F similar to that of β-Ga. Figure 5c compares $\alpha^2F(\omega)$ and the

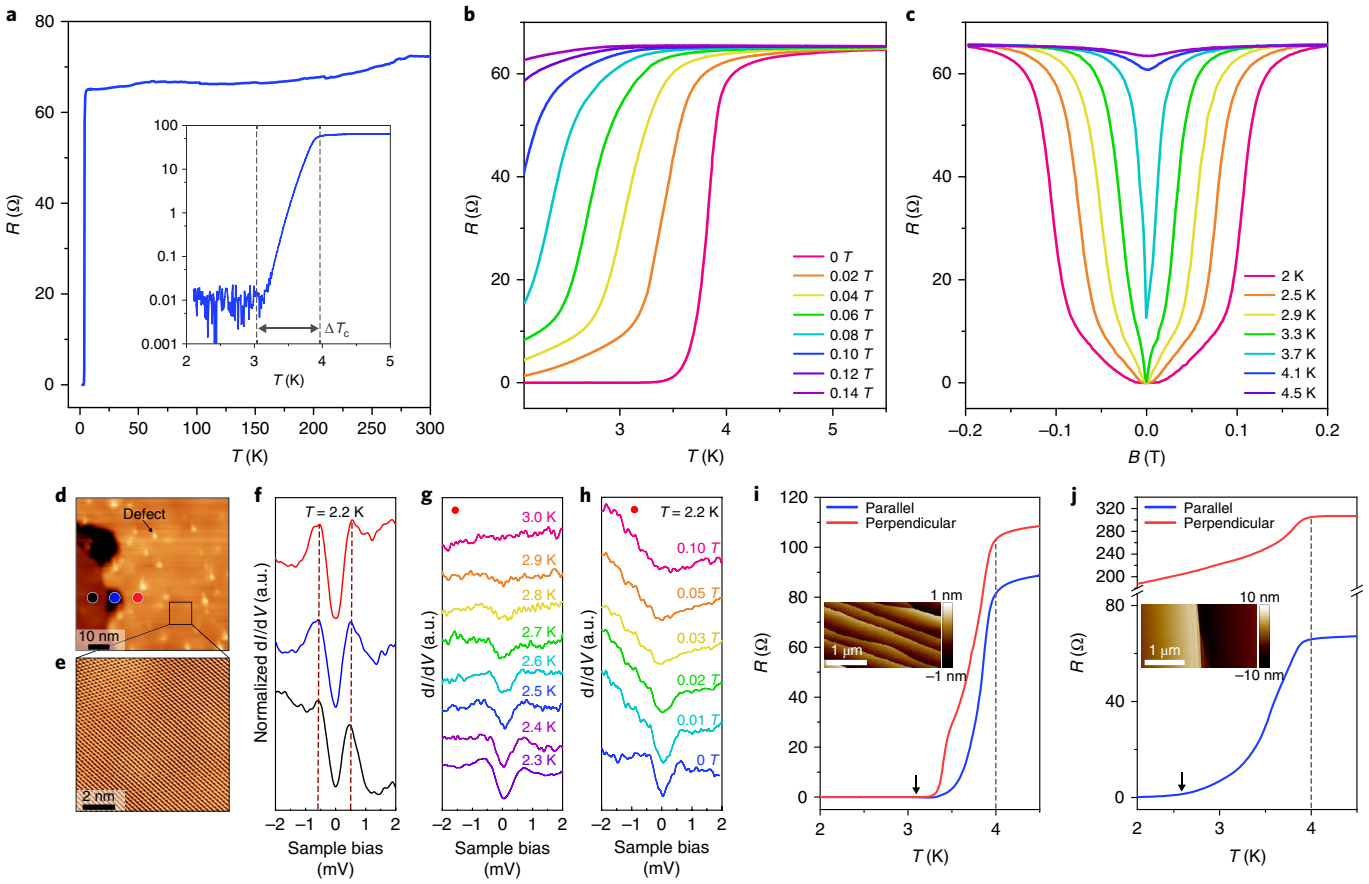

Fig. 4 | Superconductivity in 2D Ga grown via CHet. a, Zero-field $R(T)$ curve for an optimized 2D Ga film (O_2/He plasma-treated EG, small-step, parallel configuration) from 300 K to 2 K. Inset of **a**, log-scale plot from 5 K to 2 K of the same curve. **b**, $R(T)$ curves showing a suppression in T_c and increase in residual resistance at 2 K with increasing out-of-plane magnetic field. **c**, Resistance versus out-of-plane magnetic field ($R(B)$) curves showing a similar suppression in the superconducting state with increasing temperature. The kink may be attributed to two superconducting phases, possibly from discrete two-layer Ga and three-layer Ga regions, step-edge interactions or distinct superconducting transitions within a three-layer Ga region. Data shown in **a**–**c** is from the same sample and measurement configuration. **d**,**e**, Large-area and atomic-resolution scanning tunnelling microscopy images of the EG surface topography, respectively. **f**, Differential conductance (dI/dV) spectra (normalized to 3.0 K spectra) taken at 2.2 K for the three different regions shown in **d**. **g**,**h**, Temperature-dependent (zero-field) and perpendicular magnetic-field-dependent (2.2 K) dI/dV spectra, respectively, of a region on the right terrace in **d**, marked by the red dot. **i**,**j**, $R(T)$ plots comparing perpendicular and parallel current directions performed on small-step and large-step samples (both using O_2/He plasma-treated EG), respectively. Black arrows indicate approximate T_c^{zero} values, and dashed lines are meant to aid the eye ($T = 4$ K line). Insets, corresponding EG/SiC step-edge morphology and height measured by atomic force microscopy.

cumulative electron–phonon coupling strength $\lambda(\omega)$ to the projected phonon DOS for the three individual Ga layers and the interfacial Si atom. The dominant contributions to the overall $\lambda = 1.62$ come from Ga vibrations below 120 cm^{-1}, with modest evidence near 180 cm^{-1} for distinct coupling channels specific to the (more-covalent) lower layers of Ga and little sign of involvement from the interfacial Si. This result contrasts with previous reports attributing 2D superconductivity to interfacial bonding[34]. Figure 5d shows the momentum-resolved electron–phonon coupling[35] (λ_k) across the Ga/SiC Brillouin zone for electronic states within ±0.5 eV of the Fermi energy (Supplementary Fig. 19 provides a similar plot for a narrower energy range). Large contributions to λ_k come from electron pockets near the two symmetry-inequivalent K points. Further decomposition of $\lambda_{k=K}$ by phonon wavevectors shows that the strongest contributions arise from intervalley scattering between the two K valleys (see discussion on Supplementary Figs. 20,21). Interestingly, this reciprocal-space structure to the coupling is similar to that of MoS_2, but here we have a *p*-block metal (with a large companion near-circular nearly free-electron Fermi surface) with a small but crucial Fermi surface manifold of doped semiconductor character. A set of six pockets is indeed clearly seen in the ARPES measurement in Fig. 3c, 30° rotated from the EG Dirac points; these correspond to pockets near K in Fig. 3b,e, and are also similar in size to the pockets in the more accurate hybrid-functional-calculated bands of Supplementary Fig. 11 (see discussions on Supplementary Fig. 21 for details on the exact character of the pocket). The dominant contribution from these pockets is reassuring, since such strong coupling would not be expected from the more free-electron-like sheets of the Fermi surface. Using the McMillan–Allen–Dynes formula[36,37] with $\lambda = 1.62$ and μ^* from 0.1 to 0.15 yields a T_c of 3.5 to 4.1 K, in good agreement with experiment. Literature reports of the electron–phonon coupling strength in β-Ga suggest that it is also a reasonably strongly coupled superconductor[38], unlike more weakly coupled α-Ga (ref. [36]).

The large $\lambda = 1.62$ derived from the Ga states alone suggests that the EG layers are unlikely to be the driver of superconductivity in CHet-derived 2D Ga. ARPES (Fig. 3) provides further evidence towards this conclusion: the Fermi level is only 0.2–0.3 eV above the EG Dirac point, corresponding to $n \approx 8–10 \times 10^{12}$ cm^{-2}, which is ×10–100 lower than in superconducting Li-doped or Ca-intercalated

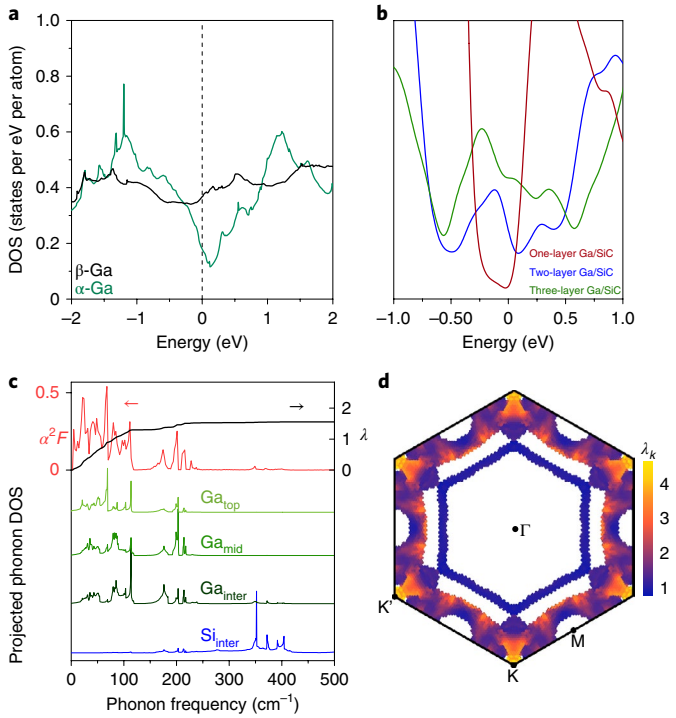

Fig. 5 | Theoretical calculations on heterostructures of graphene and 2D Ga. a, Electronic DOS versus energy DFT calculations for the two bulk phases of Ga including the stable α-Ga (low T_c) and the metastable β-Ga (high T_c) phases. **b**, DOS versus energy calculations for one- to three-layer Ga/SiC. **c**, The Eliashberg spectral function $\alpha^2F(\omega)$ (red) compared with the projected phonon DOS of the three types of Ga atoms in three-layer Ga (shades of green) and the top Si atoms at the interface (blue). The cumulative electron–phonon coupling strength $\lambda(\omega)$ is superimposed in black at the top of **c**. **d**, Momentum-resolved electron–phonon coupling λ_k shows that the dominant contribution to coupling strength λ comes from the electron pockets near the K and K′ points in the Ga Brillouin zone. The colour bar shows the range of λ_k values depicted in the image. Graphene is not included in calculations.

EG[39,40]. In those cases, superconductivity is attributed to a partially filled band near the Γ point at a much higher level of charge transfer into EG than is observed in Ga-intercalated EG. Superconductivity in low-angle twisted bilayer graphene[41] likely exhibits a different origin from that in EG/Ga, wherein the required interlayer twist is not present within the EG itself, although the environmental stability of 2D Ga coupled with the controllable thickness of EG (one- to three-layer post-intercalation) suggests prospects in mechanically stacking an additional (twisted) graphene monolayer onto EG and 2D Ga to create one of many hybrid superconducting systems possible based on the platform of highly stable CHet-derived 2D metals.

CHet stabilizes 2D forms of 3D metals. The overlying graphene layers utilized in CHet not only help confine the 2D metals, but also serve as a seal to prevent the oxidation of ultrathin non-noble metals, as revealed by the ability to perform extensive ex situ characterization of these materials. Whereas previously Au was arguably the only environmentally stable elemental metal, the realization of air-stable 2D heterostructures containing single-crystal, elemental metals and superconductors at the interface of EG and SiC opens the door to stabilizing diverse 2D allotropes of 3D metals and their alloys across the periodic table with potentially novel properties, all of which are candidates for incorporation into advanced multicomponent heterostructures for next-generation quantum[42], photonic[43] and electronic applications.

Online content

Any methods, additional references, Nature Research reporting summaries, source data, extended data, supplementary information, acknowledgements, peer review information; details of author contributions and competing interests; and statements of data and code availability are available at https://doi.org/10.1038/s41563-020-0631-x.

Received: 26 May 2019; Accepted: 3 February 2020;
Published online: 10 March 2020

References

1. Rhodes, D., Chae, S. H., Ribeiro-Palau, R. & Hone, J. Disorder in van der Waals heterostructures of 2D materials. *Nat. Mater.* **18**, 541–549 (2019).
2. Al Balushi, Z. Y. et al. Two-dimensional gallium nitride realized via graphene encapsulation. *Nat. Mater.* **15**, 1166–1171 (2016).
3. Maniyara, R. A. et al. Tunable plasmons in ultrathin metal films. *Nat. Photon.* **13**, 328–333 (2019).
4. Shah, D., Reddy, H., Kinsey, N., Shalaev, V. M. & Boltasseva, A. Optical properties of plasmonic ultrathin TiN films. *Adv. Opt. Mater.* **5**, 1700065 (2017).
5. Riedl, C., Coletti, C. & Starke, U. Structural and electronic properties of epitaxial graphene on SiC (0001): A review of growth, characterization, transfer doping and hydrogen intercalation. *J. Phys. D Appl. Phys.* **43**, 374009 (2010).
6. Emtsev, K. V., Zakharov, A. A., Coletti, C., Forti, S. & Starke, U. Ambipolar doping in quasifree epitaxial graphene on SiC (0001) controlled by Ge intercalation. *Phys. Rev. B* **84**, 125423 (2011).
7. Gierz, I. et al. Electronic decoupling of an epitaxial graphene monolayer by gold intercalation. *Phys. Rev. B* **81**, 235408 (2010).
8. Virojanadara, C., Watcharinyanon, S., Zakharov, A. A. & Johansson, L. I. Epitaxial graphene on 6H-SiC and Li intercalation. *Phys. Rev.* **82**, 205402 (2010).
9. Subramanian, S. et al. Properties of synthetic epitaxial graphene/molybdenum disulfide lateral heterostructures. *Carbon* **125**, 551–556 (2017).
10. Moulder, J. F. & Chastain, J. *Handbook of X-ray Photoelectron Spectroscopy: a Reference Book of Standard Spectra for Identification and Interpretation of XPS Data* (Perkin-Elmer, 1992).
11. Beamson, G. & Briggs, D. *High Resolution XPS of Organic Polymers: the Scienta ESCA300 Database* (Wiley, 1992).
12. Eckmann, A. et al. Probing the nature of defects in graphene by Raman spectroscopy. *Nano Lett.* **12**, 3925–3930 (2012).
13. Vishwakarma, R. et al. Transfer free graphene growth on SiO_2 substrate at 250 °C. *Sci. Rep.* **7**, 43756 (2017).
14. Araby, M. I. et al. Graphene formation at 150 °C using indium as catalyst. *RSC Adv.* **7**, 47353–47356 (2017).
15. Fujita, J. et al. Near room temperature chemical vapor deposition of graphene with diluted methane and molten gallium catalyst. *Sci. Rep.* **7**, 12371 (2017).
16. Yi, C. et al. Evidence of plasmonic coupling in gallium nanoparticles/graphene/SiC. *Small* **8**, 2721–2730 (2012).
17. Losurdo, M. et al. Demonstrating the capability of the high-performance plasmonic gallium-graphene couple. *ACS Nano* **8**, 3031–3041 (2014).
18. Khorasaninejad, M. et al. Highly enhanced Raman scattering of graphene using plasmonic nano-structure. *Sci. Rep.* **3**, 2936 (2013).
19. Voloshina, E., Rosciszewski, K. & Paulus, B. First-principles study of the connection between structure and electronic properties of gallium. *Phys. Rev. B* **79**, 045113 (2009).
20. Ashcroft, N. W. & Mermin, N. D. *Solid State Physics* (Holt, Rinehart and Winston, 1976).
21. Yoshizawa, S., Kim, H., Hasegawa, Y. & Uchihashi, T. Disorder-induced suppression of superconductivity in the Si(111)-(7×3)-In surface: scanning tunneling microscopy study. *Phys. Rev. B* **92**, 041410 (2015).
22. Yang, L., Deslippe, J., Park, C.-H., Cohen, M. L. & Louie, S. G. Excitonic effects on the optical response of graphene and bilayer graphene. *Phys. Rev. Lett.* **103**, 186802 (2009).
23. Zhang, Y., Tan, Y.-W., Stormer, H. L. & Kim, P. Experimental observation of the quantum Hall effect and Berry's phase in graphene. *Nature* **438**, 201–204 (2005).
24. Popescu, V. & Zunger, A. Extracting E versus $\vec{k}$ effective band structure from supercell calculations on alloys and impurities. *Phys. Rev. B* **85**, 085201 (2012).
25. Gregory, W. D., Sheahen, T. P. & Cochran, J. F. Superconducting transition and critical field of pure gallium single crystals. *Phys. Rev.* **150**, 315–321 (1966).
26. Chen, T. T., Chen, J. T., Leslie, J. D. & Smith, H. J. T. Phonon spectrum of superconducting amorphous bismuth and gallium by electron tunneling. *Phys. Rev. Lett.* **22**, 526–530 (1969).

27. Wühl, H., Jackson, J. E. & Briscoe, C. V. Superconducting tunneling in the low-temperature phases of gallium. *Phys. Rev. Lett.* **20**, 1496–1499 (1968).
28. Parr, H. & Feder, J. Superconductivity in β-phase gallium. *Phys. Rev. B* **7**, 166–181 (1973).
29. Werthamer, N. R. Theory of the superconducting transition temperature and energy gap function of superposed metal films. *Phys. Rev.* **132**, 2440–2445 (1963).
30. Reyren, N. et al. Superconducting interfaces between insulating oxides. *Science* **317**, 1196–1199 (2007).
31. Oliveira, M. H. Jr, Schumann, T., Ramsteiner, M., Lopes, J. M. J. & Riechert, H. Influence of the silicon carbide surface morphology on the epitaxial graphene formation. *Appl. Phys. Lett.* **99**, 111901 (2011).
32. Kruskopf, M. et al. A morphology study on the epitaxial growth of graphene and its buffer layer. *Thin Solid Films* **659**, 7–15 (2018).
33. Kruskopf, M. et al. Comeback of epitaxial graphene for electronics: large-area growth of bilayer-free graphene on SiC. *2D Mater.* **3**, 041002 (2016).
34. Zhang, T. et al. Superconductivity in one-atomic-layer metal films grown on Si(111). *Nat. Phys.* **6**, 104–108 (2010).
35. Margine, E. R. & Giustino, F. Anisotropic Migdal-Eliashberg theory using Wannier functions. *Phys. Rev. B* **87**, 024505 (2013).
36. McMillan, W. L. Transition temperature of strong-coupled superconductors. *Phys. Rev.* **167**, 331–344 (1968).
37. Allen, P. B. & Dynes, R. C. Transition temperature of strong-coupled superconductors reanalyzed. *Phys. Rev. B* **12**, 905–922 (1975).
38. Garno, J. P. Simple high vacuum evaporation system with low-temperature substrate. *Rev. Sci. Instrum.* **49**, 1218–1220 (1978).
39. Ludbrook, B. M. et al. Evidence for superconductivity in Li-decorated monolayer graphene. *Proc. Natl Acad. Sci. USA* **112**, 11795–11799 (2015).
40. Ichinokura, S., Sugawara, K., Takayama, A., Takahashi, T. & Hasegawa, S. Superconducting calcium-intercalated bilayer graphene. *ACS Nano* **10**, 2761–2765 (2016).
41. Cao, Y. et al. Unconventional superconductivity in magic-angle graphene superlattices. *Nature* **556**, 43–50 (2018).
42. Fu, L. & Kane, C. L. Superconducting proximity effect and Majorana fermions at the surface of a topological insulator. *Phys. Rev. Lett.* **100**, 096407 (2008).
43. Boltasseva, A. & Shalaev, V. M. Transdimensional photonics. *ACS Photon.* **6**, 1–3 (2019).

Methods

EG synthesis and plasma treatment. EG is synthesized via silicon sublimation from the (0001) plane of semi-insulating 6H-SiC (II-VI Inc.) at 1,800 °C, 700 Torr Ar, for 15 min (ref. [9]). EG layers were plasma treated using a Tepla M4L plasma etch tool, using 150 sccm O_2 and 50 sccm He under a pressure of 500 mTorr and power of 50 W for 60 s.

Two-dimensional metal intercalation. Metal intercalation was performed using an STF-1200 horizontal tube furnace fitted with a 1 inch outer diameter quartz tube. A custom-made alumina crucible from Robocasting Enterprises was used to hold 1 × 1 cm EG/SiC substrates, which were placed with EG layers on the Si face of SiC facing downwards, towards the inside of the crucible. Then, 30–60 mg of metallic Ga (Sigma Aldrich, 99.999%), In powder (Alfa Aesar, −325 mesh, 99.99%) or Sn granules (Alfa Aesar, 99.5%) were placed in the crucible directly beneath the EG/SiC substrate. The crucible with EG/SiC and the respective metal precursor was then loaded into the tube furnace and evacuated to ~5 mTorr. The tube was then pressurized to 300–700 Torr with Ar. At this time, the furnace was heated to 700–800 °C under a ramp rate of 20° min^{-1} and Ar flow of 50 sccm. The furnace was held at the growth temperature for 30 min, then cooled to room temperature.

XPS. XPS measurements were carried out with a Physical Electronics Versa Probe II equipped with a monochromatic Al K_α X-ray source ($h\nu = 1{,}486.7$ eV) and a concentric hemispherical analyser. High-resolution spectra were obtained over an analysis area of 200 µm at a pass energy of 29.35 eV for C 1*s*, Si 2*p*, Ga 3*d* and Ga 2*p* regions. O 1*s* regions were collected with a pass energy of 46.95 eV. The acquired spectra were fitted Lorentzian line shapes, and the asymmetric graphene peak fit was derived from exfoliated highly oriented pyrolytic graphite and H-intercalated EG reference samples. Spectra were charge referenced to this graphene peak in C 1*s* corresponding to 284.5 eV. A U 2 Tougaard background was used to fit XPS spectra.

Raman spectroscopy. Raman Spectroscopy was performed with a Horiba LabRam Raman system using a wavelength of 488 nm and a power of 4.6 mW. Spectra were acquired with an integration time of 30 s, using a grating with 600 grooves mm^{-1}.

Cross-sectional STEM. Cross-sectional samples for STEM imaging were prepared by in situ lift-out via milling in a FEI Helios NanoLab DualBeam 660 focused ion beam (FIB). Prior to the FIB, ~40/5/10 nm of SiO_2/Ti/Au was deposited via electron-beam evaporation in a Kurt J. Lesker Lab18 evaporator, to improve the contrast during STEM imaging at low magnifications. Cross sections were prepared using a Ga^+ ion beam at 30 kV, then stepped down to 1 kV to avoid ion-beam damage to the sample surface.

High-resolution STEM of sample cross sections was performed in a FEI dual aberration-corrected Titan3 G2 60–300 S/TEM at 200 kV using a high-angle annular dark-field (HAADF) detector. The HAADF detector (Fischione) had a collection angle of 51–300 mrad for Z-contrast imaging. A beam current of 70 pA, beam convergence of 30 mrad (C2 aperture of 70 µm) and camera length of 115 mm were used for STEM image acquisition. The STEM energy-dispersive X-ray spectroscopy (EDS) maps were collected using the superX EDS system, which has four EDS detectors surrounding the sample.

LEED. LEED measurements of EG/Ga/SiC, EG/In/SiC and EG/Sn/SiC samples were performed using LEED spectrometer BDL800IR-MCP manufactured by OCI Vacuum Microengineering. Samples were first degassed at 200 °C for 30 min under ultrahigh vacuum to desorb surface moisture and contaminants. LEED patterns were then acquired at room temperature using constant primary beam currents of 10 nA and beam energies of 50 eV–250 eV, in 1 eV steps.

ARPES. ARPES measurements were performed at the Microscopic and Electronic STRucture Observatory (MAESTRO) beamline at the Advanced Light Source at Lawrence Berkeley National Lab. The sample was annealed at 550 K for 30 min in the end-station before measurements to remove adsorbates from the transfer of the sample through air. Measurements of EG/Ga/SiC and Gr/In/SiC structures were performed using a photon energy of 140 eV and 110 eV, respectively. Photoemission spectra were collected by moving the sample around one angle while using the angle-resolved mode of a Scienta R4000 electron analyser for the collection of the other angular axis.

Transport measurements and T_c, B_c and T_{BKT} extraction. Transport measurements were carried out in a Quantum Design physical property measurement system (PPMS). Contacts were made to the EG/Ga heterostructure by lightly scratching the film surface with a diamond scribe or tweezers, and then lightly pressing or soldering In dots onto the scratched region. This was done in a casual attempt to make side contact to the 2D Ga. In dots were arrayed in a standard co-linear four-point-probe configuration with contact pitch on the order of hundreds of micrometres. All resistance measurements were made with an excitation current of 1 µA. T_c^{onset} is defined as the intersection of the linear extrapolations of the transition and normal regions. The linear fit for the transition region is the region of maximum slope, which is consistent for the entire transition width as seen in the log plot inset in Fig. 4a. $T_c(0.5R_N)$ is defined as the temperature at which the sample reaches half of its normal resistance. T_c^{zero} is defined as the temperature at which resistance effectively reaches a zero-resistance state (the noise floor of the PPMS system, ~0.01 Ω). The transition width ΔT_c is defined as the change in temperature between the T_c^{onset} and T_c^{zero} values. Various T_c values are provided to help in comparisons with other works in the literature, which may use different values. Critical field $B_{c2}(0.9R_N)$ is defined as the magnetic field at which the sample reaches 90% of its normal resistance. Coherence length is estimated from $B_{c2}(T) = \frac{\Phi}{2\pi\xi^2}$ where Φ is the flux quantum.

Scanning tunnelling spectroscopy/microscopy. Ga-intercalated EG/SiC was studied using an ultrahigh-vacuum low-temperature scanning tunnelling microscope with an in situ out-of-plane magnetic field at the Center for Nanophase Materials Sciences at Oak Ridge National Laboratory. The sample was preheated to 200 °C to remove surface adsorbates at ultrahigh vacuum with a base pressure of 2×10^{-10} Torr before transferring in situ to the scanning tunnelling microscope stage. Scanning tunnelling microscopy or spectroscopy was conducted using a mechanically cut Pt–Ir tip. All Pt–Ir tips were conditioned and checked using a clean Au (111) surface before each measurement. Topographic images were acquired in constant-current mode with the bias voltage applied to the samples. All the spectroscopies were obtained using the lock-in technique with the bias modulation at 973 Hz. The scanning tunnelling microscopy image in Fig. 4d was taken at $V_b = 10$ mV and $I_t = 400$ pA. The image in Fig. 4e was taken at $V_b = -100$ mV, and $I_t = 100$ pA. The dI/dV spectra in Fig. 4f–h were measured at $V_b = 5$ mV, $I_t = 400$ pA and $\Delta V = 0.1$ mV.

Theory.

i. Graphene defect generation/passivation and Ga adsorption: All DFT calculations investigating the role of plasma treatment on graphene defects and Ga intercalation were performed in Quantum Espresso[44], using projected augmented wave (PAW) pseudopotentials[45,46] and the Perdew–Burke–Ernzerhof parametrization of the generalized gradient approximation exchange-correlation functional (GGA-PBE, ref. [47,48]). A 5 × 5 × 1 Γ-centred k-point mesh was applied for Brillouin zone integration. Plane-wave expansions were truncated at an energy cut-off of 408 eV for wavefunctions and at 4,080 eV for charge densities. The Marzari–Vanderbilt cold smearing scheme[49] was applied with a broadening of 0.1 eV. Structural relaxations used the Broyden–Fletcher–Goldfarb–Shanno algorithm with a force threshold of 0.025 eV $Å^{-1}$. A vacuum layer of 20 Å was inserted in the direction normal to the graphene sheets to minimize the spurious interactions across the periodic boundary. The models in the figures were visualized using OVITO[50] and VESTA[51] software.

ii. Two-dimensional Ga phase stability and electronic structure calculations: All DFT calculations on phase stabilities and electronic structure were performed using the GGA-PBE exchange-correlation functional[47,48] and the PAW pseudopotentials[45,46]. Plane-wave expansions were truncated at an energy cut-off of 500 eV. All structural relaxations were performed using dipole corrections to the total energy[52] and to the electrostatic potential[53] in the out-of-plane direction, until the remaining forces were within 0.01 eV $Å^{-1}$. Brillouin zone samplings were performed on grids with k-point densities equivalent to that of a 20 × 20 × 1 grid for a 1 × 1 Ga/SiC unit cell. All Ga/SiC calculations were performed using seven repeating units of SiC along the *z* direction as substrate, capped by Ga from above and by H from below. Graphene/Ga/SiC calculations were performed using five repeating units along the *z* direction for a 2 × 2 graphene + $\sqrt{3}\times\sqrt{3}$ R30° Ga/SiC supercell, and three repeating units for a 5 × 5 graphene + 4 × 4 R0° Ga/SiC supercell to alleviate the computational demand of accommodating more atoms in the large supercells. Band unfolding was performed using the GPAW package[54]; all other calculations were performed by the Vienna Ab Initio Package (VASP; ref. [55]). Fermi surfaces of Ga/SiC were calculated on a 40 × 40 × 1 grid and interpolated onto a 200 × 200 × 1 grid for plotting. Band structures at the hybrid functional level were calculated using the range-separated form of Heyd, Scuseria and Ernzerhof (ref. [56]; HSE06, with a range-separation parameter of 0.2 $Å^{-1}$) and using structures relaxed at the PBE level. Self-consistent HSE06 calculations were performed on a 12 × 12 × 1 k-point grid. For the DOS of bilayer Ga in Fig. 5b, we artificially shifted E_F by 0.5 eV to account for the additional (undetermined) electron doping so that the band alignment agrees with ARPES measurements. As for the DOS calculations carried out on hexagonal two-layer and three-layer Ga/SiC, the $Ga_{Si}Ga_C$ and $Ga_{Si}Ga_CGa_C$ stacking sequences were used, respectively. The $Ga_{Si}Ga_CGa_C$ stacking sequence occupies one of the lower-energy configurations out of all the possible stacking sequences for three-layer Ga and most closely matches the band structure as directly measured in ARPES (Supplementary Figs. 10,11 and Supplementary Table 1). Thus, $Ga_{Si}Ga_C$ and $Ga_{Si}Ga_CGa_C$ stackings were used to calculate the DOS, and the $Ga_{Si}Ga_CGa_C$ stacking was used to calculate T_c (Supplementary Fig. 19a).

iii. Electron–phonon interactions: All calculations related to electron–phonon interactions were performed in a cell with only two SiC units, due to the heavy computational demand of these routines; SiC slabs were passivated from below by H atoms that are each artificially given the same mass as a Si atom (so that phonon frequencies more closely resemble that of a semi-

infinite SiC substrate). The starting-point electronic charge density was calculated on a 12×12×1 Γ-centred k-point grid. Electronic wavefunctions were then computed for a 6×6×1 grid. The phonon dispersion was calculated using density functional perturbation theory based on the same 6×6×1 grid. All computations were performed by the Quantum ESPRESSO package using the local density approximation exchange-correlation functional, Hartwigsen–Goedeker–Hutter norm-conserving pseudopotentials and a plane-wave expansion cut-off of 1,090 eV[57]. To achieve a dense sampling of electron–phonon coupling matrix elements across the Fermi surface, we constructed electronic and phonon Wannier (EPW) functions based on wavefunctions and phonon modes sampled on the coarse 6×6×1 grid and generated interpolations onto a 96×96×1 grid, as implemented by the EPW code[58,59]. Wannier functions were initialized by projecting the following orbitals onto Bloch wavefunctions: two *s* and one p_z for each Ga, one sp^3 for each Si, and one sp^3 for each C. An outer disentanglement window (one that captures all targeted bands with the chosen orbital characters) coincided with the entire energy range (Supplementary Fig. 19b)[60]. An inner window (where all Bloch states were included within the projection manifold) spanned the energy range from the lower bound of Supplementary Fig. 19b up to 1 eV above the Fermi level. See the Supplementary Information for more details on the equations and references used.

Data availability

The data that support the findings of this study are available at 10.6084/m9.figshare.c.4830711 or from the authors on reasonable request. See author contributions for specific data sets.

Code availability

Code used for computational investigations presented in this manuscript is available at gitlab.com/QEF/q-e/tree/qe-6.3 (EPW v5.0.0, Quantum Espresso v6.3) and www.vasp.at (VASP).

References

44. Giannozzi, P. et al. QUANTUM ESPRESSO: a modular and open-source software project for quantum simulations of materials. *J. Phys. Condens. Matter* **21**, 395502 (2009).
45. Kresse, G. & Joubert, D. From ultrasoft pseudopotentials to the projector augmented-wave method. *Phys. Rev. B* **59**, 1758–1775 (1999).
46. Blöchl, P. E. Projector augmented-wave method. *Phys. Rev. B* **50**, 17953–17979 (1994).
47. Perdew, J. P., Burke, K. & Ernzerhof, M. Generalized gradient approximation made simple. *Phys. Rev. Lett.* **77**, 3865–3868 (1996).
48. Perdew, J. P., Burke, K. & Ernzerhof, M. Generalized gradient approximation made simple [Phys. Rev. Lett. 77, 3865 (1996)]. *Phys. Rev. Lett.* **78**, 1396 (1997).
49. Marzari, M., Vanderbilt, D., De Vita, A. & Payne, M. C. Thermal contraction and disordering of the Al(110) surface. *Phys. Rev. Lett.* **82**, 3296–3299 (1999).
50. Stukowski, A. Visualization and analysis of atomistic simulation data with OVITO–the open visualization tool. Model. *Sim. Mater. Sci. Eng.* **18**, 015012 (2010).
51. Momma, K. & Izumi, F. *VESTA 3* for three-dimensional visualization of crystal, volumetric and morphology data. *J. Appl. Crystallogr.* **44**, 1272–1276 (2011).
52. Makov, G. & Payne, M. C. Periodic boundary conditions in calculations. *Phys. Rev. B* **51**, 4014–4022 (1995).
53. Neugebauer, J. & Scheffler, M. Adsorbate-substrate and adsorbate-adsorbate interactions of Na and K adlayers on Al(111). *Phys. Rev. B* **46**, 16067–16080 (1992).
54. Enkovaara, J. et al. Electronic structure calculations with GPAW: a real-space implementation of the projector augmented-wave method. *J. Phys. Condens. Matter* **22**, 253202 (2010).
55. Kresse, G. & Furthmüller, J. Efficient iterative schemes for total-energy calculations using a plane-wave basis set. *Phys. Rev. B* **54**, 11169–11186 (1996).
56. Heyd, J., Scuseria, G. E. & Ernzerhof, M. Hybrid functionals based on a screened Coulomb potential. *J. Chem. Phys.* **118**, 8207–8215 (2003).
57. Hartwigsen, C., Goedecker, S. & Hutter, J. Relativistic separable dual-space Gaussian pseudopotentials from H to Rn. *Phys. Rev. B* **58**, 3641–3662 (1998).
58. Noffsinger, J. et al. EPW: a program for calculating the electron–phonon coupling using maximally localized Wannier functions. *Comp. Phys. Commun.* **181**, 2140–2148 (2010).
59. Giustino, F., Cohen, M. L. & Louie, S. G. Electron-phonon interaction using Wannier functions. *Phys. Rev. B* **76**, 165108 (2007).
60. Souza, I., Marzari, N. & Vanderbilt, D. Maximally localized Wannier functions for entangled energy bands. *Phys. Rev. B* **65**, 035109 (2001).

Acknowledgements

Funding for this work was provided by the Northrop Grumman Mission Systems' University Research Program, Semiconductor Research Corporation Intel/Global Research Collaboration Fellowship Program, task 2741.001, National Science Foundation (NSF) CAREER Awards 1453924 and 1847811, the Chinese Scholarship Council, an Alfred P. Sloan Research Fellowship, NSF DMR-1708972 and 1808900, and the 2D Crystal Consortium NSF Materials Innovation Platform under cooperative agreement DMR-1539916. A portion of this research was conducted at the Center for Nanophase Materials Sciences, which is a DOE Office of Science User Facility, and at the Pennsylvania State University Materials Research Institute's Material Characterization Laboratory. This research used resources of the Advanced Light Source, which is a DOE Office of Science User Facility under contract no. DE-AC02-05CH11231. We acknowledge Haiying Wang for help with STEM sample cross-section preparation via FIB; Vince Bojan, Nabil Bassim and Heshem Elsherif for help with AES; and Max Wetherington for Raman spectroscopy support.

Author contributions

N.B, B.B., Y.W., V.C. and J.A.R. wrote the paper with input from the co-authors. N.B. performed CHet and XPS characterization and assisted in the Raman spectroscopy and SEM characterization. B.B performed the Raman spectroscopy and SEM characterization and assisted in sample preparation and electrical characterization. Y.W. performed DFT modelling of graphene/Ga/SiC heterostructures in consultation with V.C. with input from J.Z., B.B., N.B. and J.A.R.; J.J. performed electrical measurements under the direction of C.Z.C. with input from B.B and J.Z.; R.K., A.B. and C.J. performed ARPES measurements under the direction of E.R.; N.N. performed graphene defect modelling under the direction of A.v.D.; and K.W. performed cross-sectional STEM imaging. M.K. and W.K. prepared the LEED instrument for EG/metal/SiC samples, and M.K. performed the LEED measurements. A.D.L.F.D. assisted with CHet and material characterization. C.D. and S.S. performed the EG synthesis under the direction of J.A.R.; J.S. assisted in XPS data analysis. M.F., Q.Z., G.Z. and A.P.L. performed the scanning probe characterization. Y.W.C. assisted with electrical measurements under the direction of J.Z.

Competing interests

The authors declare no competing interests.

Additional information

Supplementary information is available for this paper at https://doi.org/10.1038/s41563-020-0631-x.

Correspondence and requests for materials should be addressed to J.A.R.

Reprints and permissions information is available at www.nature.com/reprints.